4-2012

The Variation of Hydrogen Concentration in Ni/MgH Thin Film with Temperature

Rex Nyadaufe Taibu
Western Michigan University

THE VARIATION OF HYDROGEN CONCENTRATION IN Ni/MgH THIN FILM WITH TEMPERATURE

by

Rex Nyadaufe Taibu

A Thesis
Submitted to the
Faculty of The Graduate College
in partial fulfillment of the
requirements for the
Degree of Master of Arts
Department of Physics
Advisor: Asghar Kayan, Ph.D.

Western Michigan University
Kalamazoo, Michigan
April 2012

THE VARIATION OF HYDROGEN CONCENTRATION IN Ni/MgH THIN FILM WITH TEMPERATURE

Rex Nyadaufe Taibu, M.A.

Western Michigan University, 2012

The thermal stability of Ni/MgH thin film deposited on Si substrate by Unbalanced Magnetron Physical Vapor Deposition has been investigated using Ion Beam analysis (IBA) techniques. Rutherford Backscattering Spectrometry (RBS) and Non-Rutherford Backscattering Spectrometry (NRBS) have been used to find the composition of Magnesium, Nickel and Oxygen. Elastic Recoil Detection Analysis (ERDA) has been used to determine the concentration of hydrogen at each level of heating. Heating was done in the Ultra High Vacuum (UHV) environment using a non gassy button heater. Ni/MgH sample had lost most of its hydrogen after being heated to a temperature of about 125°C in vacuum. However, the onset temperature of hydrogen loss from the sample was found to be within 21°C and 50°C. The interface regions between the film and the substrate and between Ni and MgH layers were unaffected by this operation.

ACKNOWLEDGMENTS

I am heartily thankful to my supervisor, Dr. Asghar Kayani, whose encouragement, guidance and support from the beginning to the end level enabled me to develop an understanding of the subject. I am also indebted to my committee members Dr. David Schuster and Dr. Paul Pancella for their constructive criticism in making this work better. I am so thankful to my wife Hannah and my daughter Shania for their emotional support during the project. Lastly, I offer my regards and blessings to all of those who supported me in any respect during the completion of the project.

Rex Nyadaufe Taibu

TABLE OF CONTENTS

Table of Contents-continued

CHAPTER

Table of Contents-continued

LIST OF FIGURES

CHAPTER I

BACKGROUND

1.1 The Need for Alternative Sources of Energy

The need for alternative energy sources that are environmentally friendly has led to an intensive research in hydrogen storage materials and better designs of fuel cells that could reduce dependency on oil. There is need for safer and better hydrogen storage material for fuel cells which has minimal negative impact on the environment as is with fossil fuels used presently [1]. The search for a better hydrogen storage material can best be explored if the basic idea of the operation of hydrogen fuel cells is known.

1.2 The Basic Operation of Hydrogen Fuel Cells [1]

Hydrogen fuel cells require hydrogen to deliver electrical energy. Electrical energy is generated from the combustion of hydrogen, i.e.: $2H_2 + O_2 \longrightarrow 2H_2O$. This reaction goes in two stages. The first stage occurs at the anode (Figure 1) where hydrogen gas from the storage container ionizes into protons and electrons. The direction of arrows outside the fuel cell in Figure 1 shows that the liberated electrons pass through the load to the cathode. At the same time the protons complete the circuit by passing through the electrolyte. The electrolyte is chosen so that it favors proton transfer. The second stage occurs when the protons and the electrons at the

cathode react with oxygen to form water. The overall process delivers power to the load ready for use.

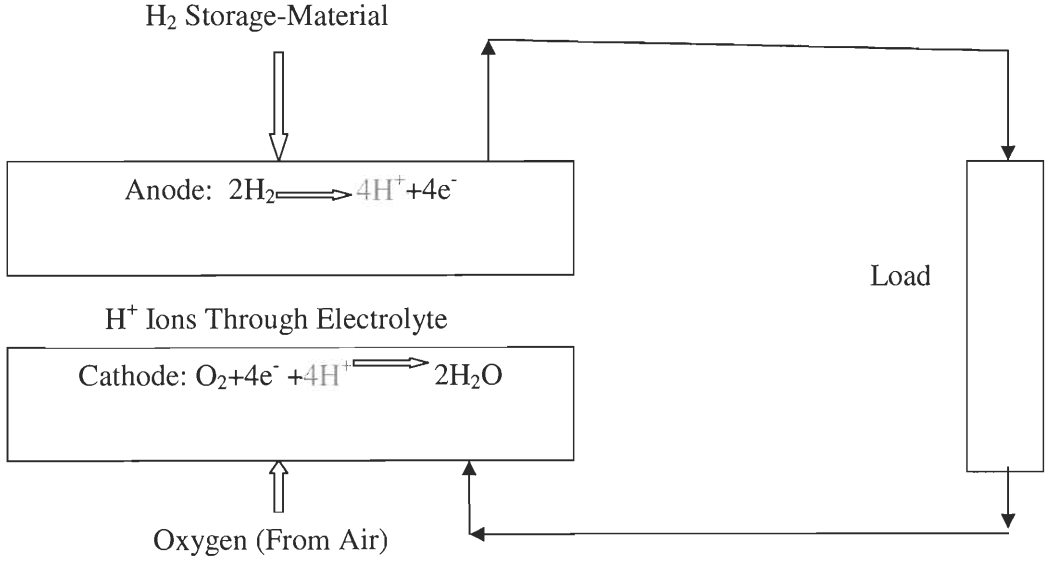

Figure 1: The Basic Operation of a Hydrogen Fuel Cell

The output voltage can be enhanced in several ways. One of them is to increase the amount of hydrogen available for the reaction. This can be done by heating the solid hydrogen storage material or adding a catalyst to it for easy hydrogen dissociation. In this study, the effect of heating a solid hydrogen material and addition of a catalyst will be investigated.

1.3 Hydrogen Storage Materials

The advances in producing safer hydrogen storage materials for fuels cells have faced several problems. For example, hydrogen-based fuel cells for vehicular transportation have faced problems regarding "on board" storage [2]. Condensed

hydrogen is very expensive to produce and maintain [3]. Pressurized or liquefied hydrogen in vehicles poses safety concerns on the high probability of combustion that may result. Hydrogen is difficult and costly to store either in liquid or gas form because of its low boiling point (-252.87^{o}C) and low density in the gaseous state (0.08988g/L at 1atm) [4]. While liquid hydrogen requires additional costs for refrigeration, gaseous hydrogen is limited by the weight of the canisters and leakage problems are likely to be of primary concern [4, 22]. Thus both liquid and gas hydrogen storage pose safety concerns for vehicular use.

Several studies are being conducted to meet the US Department of Energy (DOE) vision for the ideal hydrogen storage materials that are both environmentally and economically friendly [5]. According to DOE, there is a need for hydrogen storage materials with hydrogen storage capacity of 6.5wt% and 65g/L hydrogen available at relatively low decomposition temperature between 60 and 120^{o}C for commercial purposes [4]. Work is still in progress to better meet the DOE vision.

Weifang Luo[2], 2004 reports that hydrogen storage in solid materials has long been recognized as one of the most practical approaches for on board storage. Several solid state materials have been investigated on their ability to absorb and desorb hydrogen. These solid state materials include carbon structures, metals and metal alloys.

1.4 Metal Hydrides

Several metal hydrides have been investigated, with much effort driven towards finding a better hydride with good hydrogen absorption and desorption

properties at reasonably low temperatures. A number of studies have also focused on maximizing the capacity of hydrogen in metal hydrides [4, 7, 11]. Most of these studies agree that a good metal hydride should have a relatively high capacity of hydrogen.

Hydrogen readily combines with metals to form metal hydrides; it is better and safer to store it in solid state rather than liquid or gaseous state. Moreover, solid state storage materials have relatively higher hydrogen storage capacity than gas and liquid storage materials. For example; 6.5 hydrogen atoms/cm^3 in MgH_2, 0.99 hydrogen atoms/cm^3 in hydrogen gas and 4.2 hydrogen atoms/cm^3 in liquid hydrogen [22]. Solid state storage materials are also safer because hydrogen does not easily detach itself from metal bonds for reactions, unlike in gas or liquid.

Hydrogen can attach to a metal either directly or indirectly. Direct combination refers to a hydrogen molecule combining with a metal to yield a metal hydride species only; indirect combination refers to water molecule combining with a metal yielding metal hydride and hydroxyl species. These two processes form two different kinds of hydrides: (i) α-phase at which only some hydrogen is absorbed and (ii) β- phase at which the hydride is fully formed [4].

1.5 Magnesium-Based Hydrides

Hydrides of magnesium hydride are advantageous because they are light for onboard use and relatively inexpensive [6]; moreover, Mg is abundant in nature as well. Mg-based hydrides also possess attractive qualities such as: heat resistance, vibration absorbance, reversibility and recyclability [24] and has a good hydrogen

capacity up to 7.6wt% for on board application [4]. The major drawback of magnesium hydride is its high desorption temperature (above 300°C), which is related to the high stability of the Mg–H bonds [6]. Un-milled magnesium hydride keeps the hydrogen more stable than milled or catalyzed hydrides. High reactivity toward air and oxygen is an additional limitation [4].

Improvement to these limitations is achieved in bulk materials through ball-milling and addition of catalysts to MgH_2. Although a number of metals can be used for hydrogen absorption, studies show that magnesium is an ideal metal not only for its reasonable weight and inexpensiveness but also its hydrogen storage capacity.

1.6 The Kinetics of Hydrogen in Metal Hydrides

Several factors affect the diffusion kinetics of hydrogen in metal hydrides that includes hydrogenation and oxidation [4]. The formation of a magnesium hydride layer encloses the bulk material, there by slowing down the absorption and desorption processes. Hydrogen diffusion is also hindered by the oxidation of the metal. Oxidation takes bonding sites for hydrogen, in this case forming MgO. The diffusion kinetics of hydrogen in metal hydrides is enhanced by adding catalysts as well as ball milling of the bulk materials which creates a large surface area of the material [7, 23]. Catalysts enable H_2 to dissociate in atomic H. Hydrogen sorption properties in magnesium hydride have been found to improve significantly in energetic ball milled hydrides [9]. Despite the introduction of catalysts and ball milling techniques to metal hydrides, the ideal operating temperature is yet to be achieved [4].

Although most of the work has been carried out using bulk materials, our approach to understand the diffusion kinetics and thermal stability of H in these materials is to use thin films. Using thin films, the investigations of these kinds offer many advantages, such as (a) novel electron and electromagnetic spectroscopic techniques can be used to characterize the material and (b) ion beam analysis techniques can be used to precisely quantify the uptake and the transport of H. My work as part of this big project is to find the onset temperature and thermal stability of H in MgH thin film.

CHAPTER II

SAMPLE PREPARATION

For this study, thin film of MgH was deposited by physical vapor deposition (PVD) process using magnetron sputtering technique. The schematic diagram of PVD deposition chamber is given in Figure 2[11].

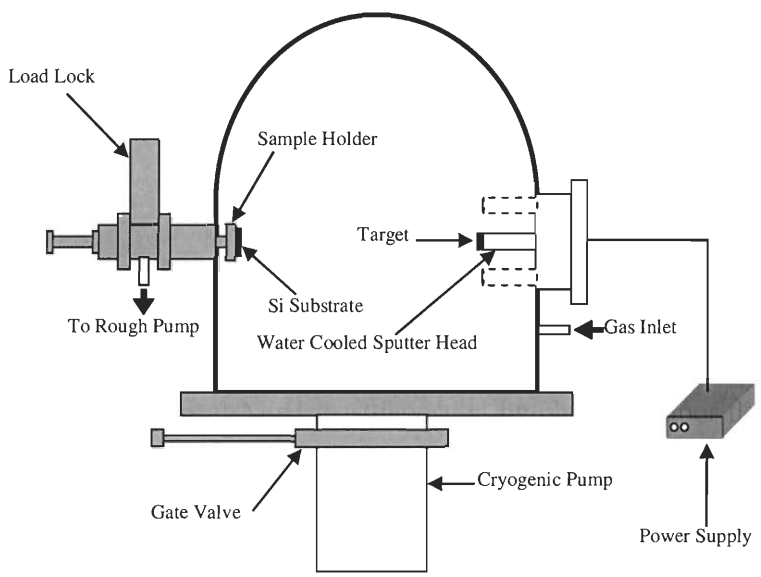

Figure 2: Diagram of a UHV Magnetron Sputtering Deposition Chamber

2.1 The Physical Vapor Deposition (PVD) System

The PVD is an industrial scale process to deposit thin film/coatings of target materials on suitable substrates. Magnetron sputtering thin film deposition is a

process in which a target material is sputtered using sputtering gas like Ar, the form of atoms, ions or molecules and is transported as low pressure plasma to the substrate where it condenses [10]. PVD processes can be used to deposit thin films or coatings of elements and alloys as well as compounds using reactive deposition processes [10]. In reactive deposition processes, compounds are formed by the reaction of the depositing material with an ambient gas environment such hydrogen or nitrogen. In industry, the PVD coating technology is applied in the fabrication of materials such as lock hardware, kitchen hardware, watches and clocks [10]. In this study, the PVD process has been used to make thin films composed of magnesium, hydrogen and nickel; which were then analyzed using ion beam analysis.

2.2 Technical Details of the PVD System Used (Figure 2)

The PVD deposition is carried out in a cylindrical stainless steel (20cm in diameter) which has an Ultra High Vacuum (UHV) chamber. Vacuum in the chamber is obtained using cryogenic pump. A mechanical pump is connected with the chamber to pump the chamber to rough pressure after which cryogenic pump takes over. Pressure inside the chamber is measured using an ion gauge. The chamber is fitted with three 1-inch unbalanced magnetron sputter heads connected to two DC and one RF power supplies. Each sputter head has its own shutter. These shutters are operated from outside the chamber and are used to deposit multilayer coatings on the substrate. The gases for sputtering and reactive deposition are introduced into the chamber using precision mass flow controllers. Argon was used to sputter the chosen metal onto the target while hydrogen was used to dilute the growth plasma to have reactive

deposition Sample holder along with the substrate is inserted into the chamber via load lock. This ensures that the main deposition chamber remains clean.

2.3 Details of the Deposition

For deposition, a silicon substrate was mounted on a 5.6cm circular diameter stainless steel sample holder and inserted into the chamber via load lock. Inside the deposition chamber the distance between the substrate holder and the sputter heads was fixed at 20cm throughout the deposition process. Two sputter head mounted with Mg and Ni targets were connected with the direct current (DC) power supplies. Power supplies were set at 31 watts. For the deposition, 200 sccm of argon and 10 sccm of hydrogen were introduced in the chamber via separate precision mass flow controllers. An argon/hydrogen atmosphere was used to deposit magnesium hydride (MgH) onto the silicon substrate. The base pressure in the deposition chamber was in the lower 10^{-8} Torr range which was raised to 6 mTorr working pressure.

The deposition for the MgH sample was carried out for 30 minutes. After the MgH deposition, sample was allowed to cool down for 10 min after which nickel was deposited for 7.5 minutes on top of the MgH layer. Ni layer was deposited to cap the MgH sample to prevent any possible oxidation when the sample is exposed to air. Moreover, Ni is used as a catalyst for the molecular hydrogen to dissociate into atomic. The choice of Ni on MgH was used to mimic the situation where Mg has absorbed H. Thickness of the film is determined by time of sample deposition and the power of the gun among other factors. The time for deposition was chosen based on the knowledge of previous similar sample deposition experiments [11].

CHAPTER III

ION BEAM ANALYSIS TECHNIQUES

In this study, three ion beam analysis techniques have been employed; Rutherford Backscattering Spectrometry (RBS), Non Rutherford backscattering Spectrometry (NRBS) and Elastic recoil Detection Analysis (ERDA). These techniques provide powerful tools for quantitative analysis of thin films and depth profiling of near surface layers in solids. They can provide information on composition and layer thickness of the sample [12].

3.1 Rutherford Backscattering Spectrometry (RBS)

RBS is one of the most widely and commonly applied techniques in surface analysis of solids. It is quantitative and very precise [14, 13]. RBS can quantitatively determine the composition of a material and obtain a profile of individual elements vs. depth. RBS does not need reference samples and same is true for NRBS. It is nondestructive and has a good depth resolution of the order of several nm. RBS is very sensitive to heavy elements and is less sensitive to for light elements [15] which can be detected by other techniques such as NRBS, nuclear reaction analysis (NRA) or Elastic Recoil Detection Analysis (ERDA).

In RBS, a sample is bombarded with a beam of ions with mass M_1 and a known energy, E_1 (e.g. He^{++} particles, typically 0.5-4 MeV) [15, 14]. Ions undergoing elastic Coulomb collisions are recorded by an energy sensitive solid state detector

positioned at a scattering angle θ (Figure 3). In Figure 3, α is the angle between the incident beam and the normal to the target surface (incident angle), β is the angle between the normal and the reflected beam (exit angle). RBS relies on the fact that the energy, E_2 of the backscattered particle, depends on the energy E_1 before the collision, the incident mass M_1, the target mass M_2 and the scattering angle θ.

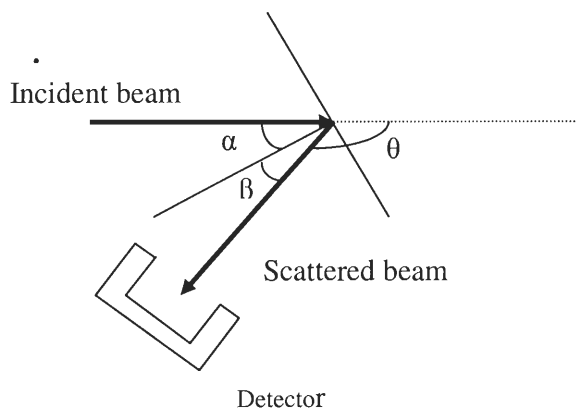

Figure 3: RBS Geometry

The latter statement comes from the conservation of energy and momentum for particles under consideration. Described mathematically,

$$E_2 = E_1\left[\frac{\left(M_2^2 - M_1^2\sin^2\theta\right)^{1/2} + M_1\cos\theta}{M_1 + M_2}\right]^2 \qquad (1)\ [14]$$

Equation 1 can be written as $E_2=KE_1$, where K is the kinematic factor. With K, Energy loss of the backscattered ions provides signature of the target atom energy. It can be deduced from equation 1 above that incident particles on a heavy particle lose less energy than that incident on a relatively lower atomic mass unit. The kinematic

factor helps distinguish different targets in a sample for a particular projectile however; mass resolution becomes nearly impossible for very heavy target particles. For example, ^{181}Ta and ^{201}Hg can hardly be resolved with MeV He beam appropriate for RBS.

The energy scale in figure 4 (RBS example [14]) is proportional to the kinematic factor for a given projectile energy. Hence the x axis is proportional to the kinematic factor which in turn distinguishes masses in the target sample.

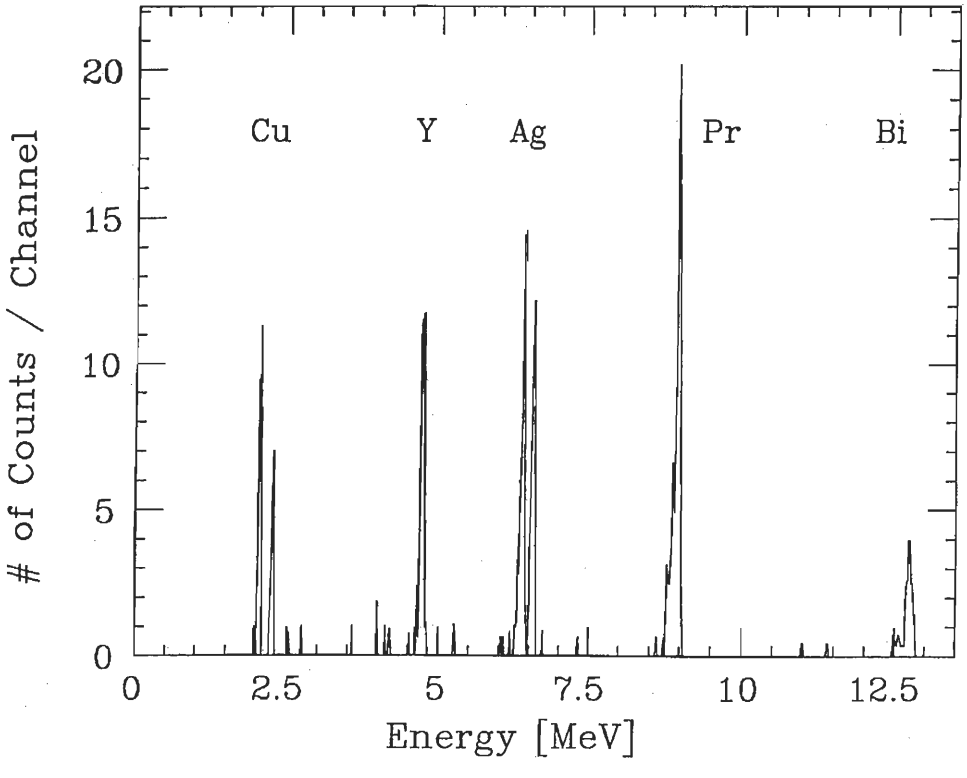

Figure 4: RBS Example Demonstrating Mass Discrimination (Projectile: 25 MeV ^{35}Cl; Target: Thin Layers of Cu, Y, Ag, Pr, Bi. Isotopes of Cu and Ag are Resolved)

The probability of scattering (assuming elastic Coulomb collision) of the projectile on a given target is described by Rutherford cross-section. This is mathematically derived and is given in the laboratory inertial reference frame by:

$$\sigma_R(E,\theta) = 4\left(\frac{Z_1 Z_2 e^2}{4E}\right)^2 \frac{\left\{\left(M_2^2 - M_1^2 \sin^2\theta\right)^{1/2} + M_2 \cos\theta\right\}^2}{M_2 \sin^4\theta\left(M_2^2 - M_1^2 \sin^2\theta\right)^{1/2}} \qquad (2)\ [20]$$

θ is the scattering angle, Z_1 and M_1 are the nuclear charge and the mass of the projectile, respectively, and Z_2 and M_2 are the nuclear charge and the mass of the target atom, respectively. E is the energy of the incident ion while e is the electronic charge. σ_R is also called the differential cross-section in the laboratory system. This expression indicates that the probability of scattering is proportional to the square of the atomic number of the target atom and inversely proportional to the square of the incident ion energy. This explains why RBS is more sensitive to heavier atoms than to lighter ones. In this study, RBS has been more sensitive to Si than Mg. Also RBS has been more sensitive to Mg than it has been to O, forcing us to use Non-Rutherford Backscattering Spectrometry for easier modeling of oxygen spectra.

3.2 Non-Rutherford Backscattering Spectrometry (NRBS)

The actual cross section (from experiments) deviates from Rutherford cross section at both low and high incident beam energies [15]. The low-energy departures are caused by partial screening of the nuclear charges by the electron shells surrounding both nuclei while at high energies the cross-sections deviate from

Rutherford due to the influence of the nuclear force. Since the cross section of Silicon is larger than that of Mg and O, it is challenging to detect and simulate the presence of these elements (peaks) in a sample using the traditional RBS with silicon as a substrate. To better recognize and simulate these elements, in this experiment we used NRBS technique which takes into account the deviations due to inelastic collisions which may be due to nuclear effects at low and high energies. Since most of the interaction processes are very well explored during the many decades of nuclear research, the analysis by computer soft ware is often straightforward and completely quantitative[14].

3.3 Scattering Geometries [15]

In this study the IBM scattering geometry (Figure 5[15]) has been used for all ion beam measurements. The incident beam, exit beam and surface normal of the sample are in the same plane, with

$$\alpha + \beta + \theta = 180^{\circ} \tag{3}$$

Where α is the angle between the incident beam and the normal to the target surface (incident angle), β is the angle between the normal and the reflected beam (exit angle) and θ is the scattering angle (Figure 5).

The Cornell geometry (Figure 4) is sometimes used for scattering. In this geometry, the incident beam, exit beam and the rotation axis of the sample are in the same plane, and

$$\cos(\beta) = -\cos(\alpha)\cos(\theta). \tag{4}$$

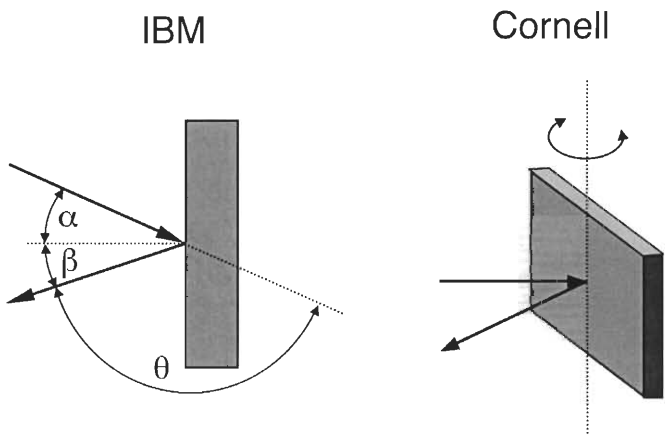

Figure 5: The IBM and the Cornell Geometry

While the IBM configuration is easy to grasp, the Cornell geometry has the advantage of combining a large scattering angle, which is desirable for optimized mass resolution, and grazing incident and exit angles, which optimizes depth resolution.

3.4 Elastic Recoil Detection Analysis (ERDA)

A heavier incident particle cannot be backscattered from a lighter target element. Instead, it recoils forward the target element. For instance, He^{++} ions and O^{4+} ions can forward recoil hydrogen. This concept is used to get information from lighter elements. Although we use the same principles as in RBS, in ERDA the information about the target is carried by the target elements themselves and not by the backscattered particles. Forward recoil is made possible by choosing grazing angle geometry. Since several particles can be recoiled to the detector, a foil is placed in

front of the detector to allow the chosen particles to pass through while blocking others (Figure 6). In this study a Mylar foil of 13 microns was used.

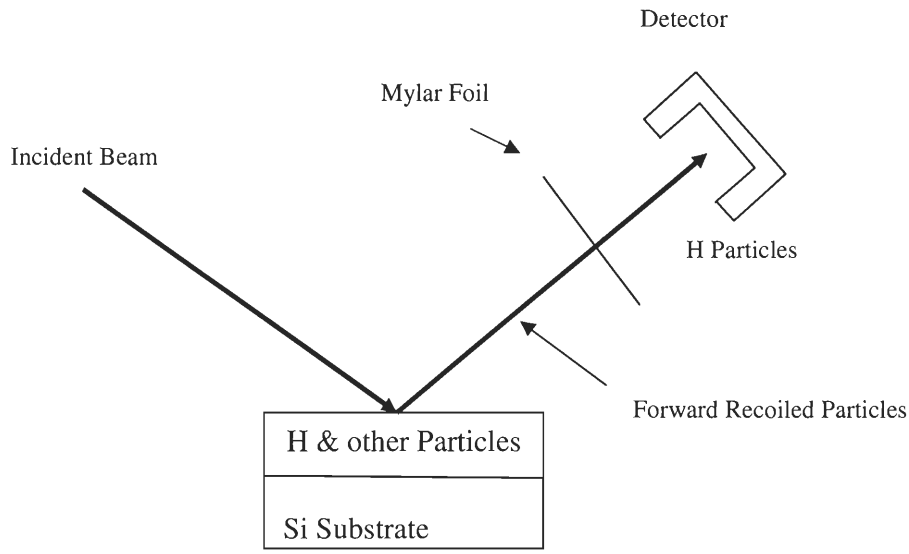

Figure 6: Elastic Recoil Detection

The great advantage of ERDA with a mass (or nuclear charge) discriminating detector is that the depth profiles of all light target elements can be obtained simultaneously well separated from each other[14]. This idea has been employed in this study to try to separate hydrogen and deuterium cross sections as we tried to see if we can add deuterium to our heated sample.

3.5 SIMNRA [16]

SIMNRA software has been used in this study to simulate the data. Simulation goes by 'try and error'. From the simulation, composition profiles can be obtained.

CHAPTER IV

THE ACCELERATOR

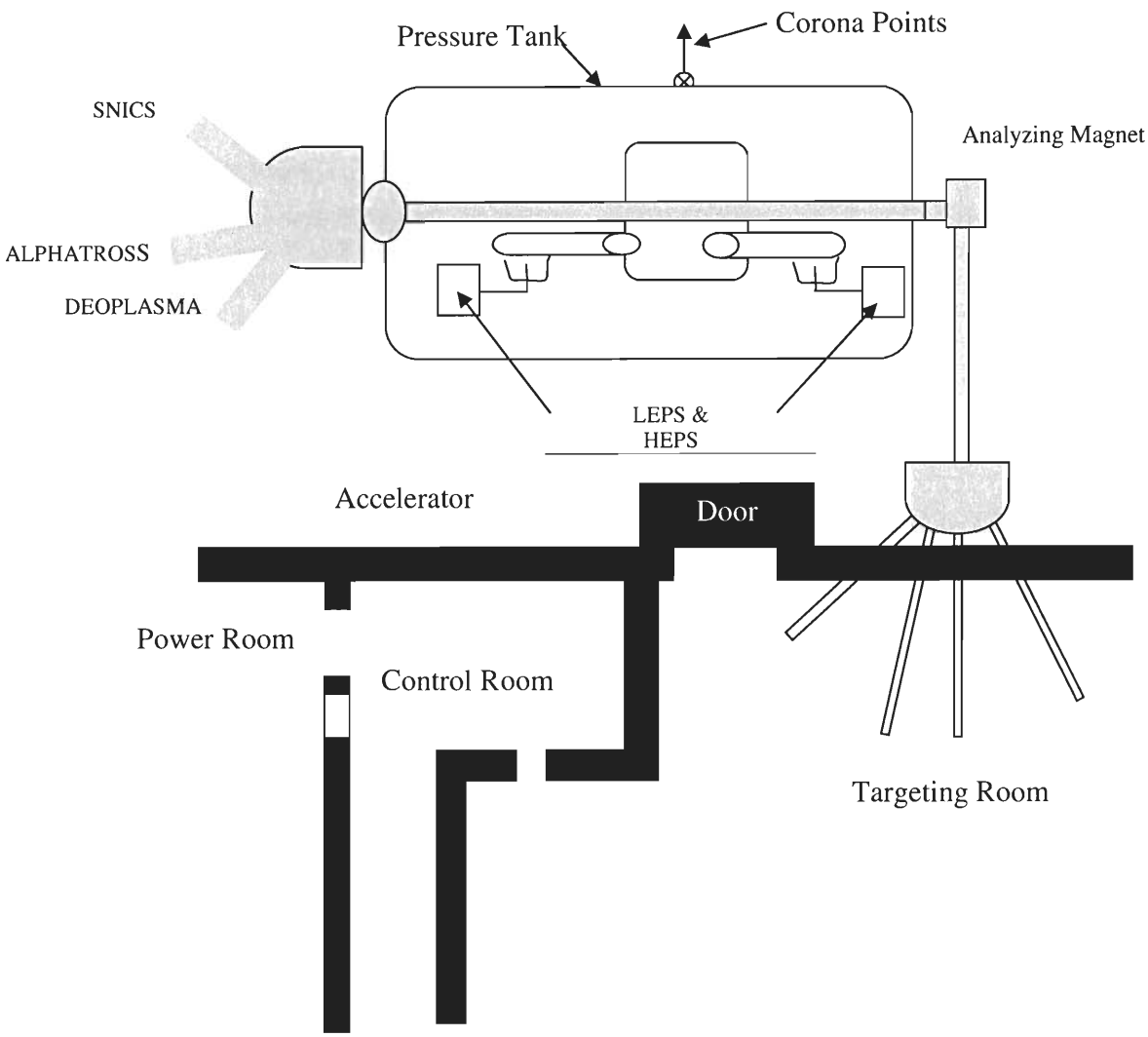

Figure 7: Diagram of a Tandem Van der Graaff Accelerator (LEPS: Low Energy Power Supply, HEPS: High Energy Power Supply)

Two major machines have been used in this study; the accelerator and the UHV physical vapor deposition system described in chapter II. The accelerator (Figure 7) has been used to provide the high energy beam necessary for the IBA techniques.

The accelerator at Western Michigan University is a 6-MV tandem Van de Graaff accelerator, which has been in continuous use for more than 31 years. Several vacuum pumps are attached throughout the beam path to ensure a clear path that does not weaken the beam as well as avoiding deflections, interactions or charge exchange.

Generally, in a Tandem accelerator, anions are extracted from the ion source and accelerated by a very high positive voltage at the geometric center of the pressurized steel tank. This stage is called the "terminal voltage" (TV). The high voltage is generated by the 'Van de Graaf generators'. The Corona system is designed so as to help maintain the TV. The corona system consists of very sharp needles mounted inside (but isolated from) a dome shaped electrode. These needles can be moved close to or far away from the terminal electrode. The area surrounding the TV is pressured to help prevent electrical discharges thereby protecting the lab personnel. In our case mixture of carbon dioxide and nitrogen is used to provide the pressure. At the TV the anions are stripped of a number of electrons and become cations. This stripping is done by oxygen gas or carbon foil. The cations are then further accelerated away from the positive TV ending up with final beam energy of (n+1) x TV where n is the number of positive charge states on the outgoing ion and, TV is the terminal voltage [21]. This implies that the Tandem accelerator accelerates the

particle twice. Knowledge of incident beam energy and the incident charge state determines the appropriate TV. Although this is the case, different charge states can be produced at the chosen fixed TV. The Analyzing Magnet (AM) helps select out the required charge state ready for use in the scattering chamber.

4.1 Ion Sources

4.1.1 SNICS: Source of Negative Ions by Cesium Sputtering (Figure 8)

Initially, we had two ion sources: the Source of Negative Ions by Cesium Sputtering (SNICS) and the duo-plasma exchange source.

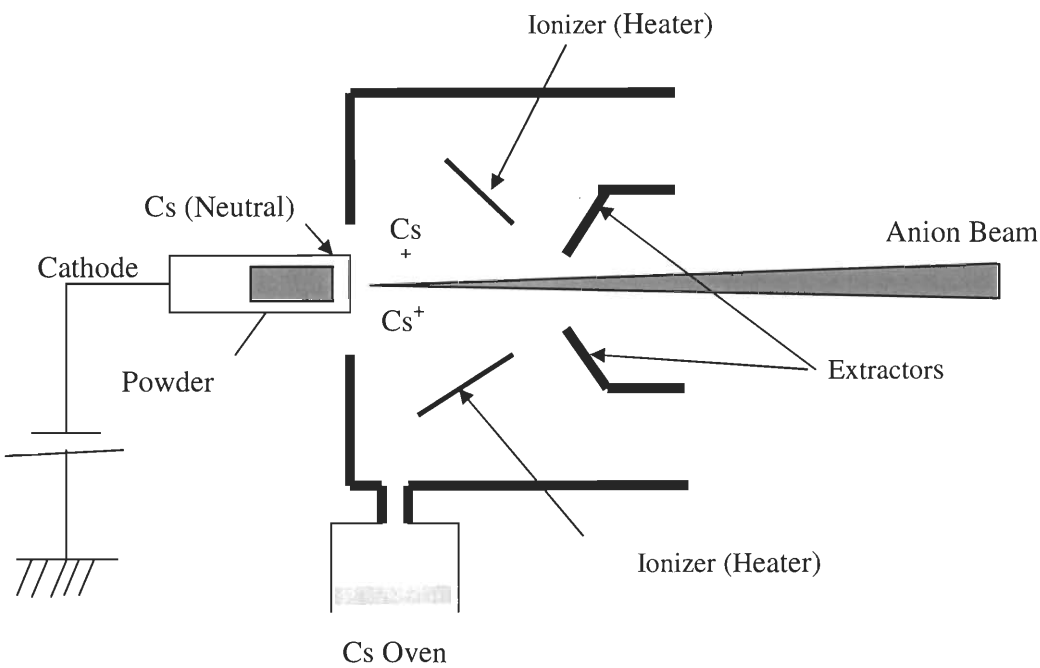

Figure 8: The Schematic Diagram of SNICS

Recently the alphatross has been added as another source of negative ions. In this study, we used SNICS to get O^{4+} and protons. We used alphatross source to get the He^{2+} beam.

4.1.2 The Principle of Operation of SNICS

Cesium is heated in the oven, forming Cs vapor which migrates into the ion source. In the ion source, the ionizer is also heated and lies at a higher temperature than the cathode. The higher temperature ionizes some of the Cs vapor while the rest of the vapor condenses at the cathode as a bulk of cesium neutral atoms (Figure 7). The ionized Cs particles accelerate towards the cathode. At the cathode, the Cs^+ penetrates the neutral cesium layer and sputters the deeper contents of the cathode (for instance, a powder of MgO). The atoms to be accelerated are incorporated in the cathode. For instance, for copper, the sputter cathode would be made of solid copper; for oxygen, magnesium oxide would be incorporated into the cathode. The sputtered particles e.g. oxygen from MgO powder picks up an electron as it escapes the neutral cesium layer forming the negative beam.

4.1.3 Alphatross Ion Source

Although the above procedure works well for many ions, there are a number of elements which do not easily form a negative ion. Helium, an inert gas, is a concrete example. The Alphatross ion source produces negative 3He or 4He beams ready to be captured at the TV in the tandem Van der Graaf accelerator. The process is slightly different from the SNICS ion source. Basically, the procedure is to produce a positive helium ion in the usual way, i.e. in much the same way as the positive Cesium ions are produced in SNICS and to pass the beam (positively charged helium ions) through a charge exchange canal containing an element such as lithium or rubidium which has a high affinity for giving up an electron. The negatively charged

helium particles are then attracted to the TV ready for further acceleration after being positively charged by the striper.

4.2 The Scattering Chamber

This is located in the target room. In this study we used the 0^{o} beam line, the beam line that goes straight from the analyzing magnet to the scattering chamber (Figure 6). The chamber is kept at a high vacuum around 10^{-7}-10^{-8} torr by a turbo and ion pumps. Within the chamber is the surface barrier Si detector is mounted on a shaft of rotary feed through. This is used for backscattering spectroscopy and Nuclear Reaction Analysis (NRA).The detector is flexible for several scattering angles. The detector for ERDA is fixed at a scattering angle of 45^{o}. The aperture diameter is the same for both RBS and ERD detectors, i.e. 3.175mm. The distance from the target to the detector is 6.82cm and 9.3242cm for RBS and ERD configuration respectively.

4.3 Data Acquisition

Figure 9 shows a schematic diagram of data acquisition electronic system from the scattering chamber. The detector is connected to the preamplifier which in turn is connected to the spectrometry amplifier. The amplifier is then connected to the Multichannel analyser (MCA). Before the beam hits the sample, it passes through the slits, collimator and then the tungsten mesh. The slit and the collimator have a function of focusing the beam as it approaches the sample. The mesh has 80% transmission. The mesh is connected to the current integrator which is linked to the counter. The counter triggers the operation of the MCA. There are two ways to measure current, (1) cylinder grounded and mesh biased and (2) cylinder at -300V and

mesh unbiased. We used the later one in this study to suppress secondary electrons which come from the beam-mesh interaction. This way we could get a reliable measurement of the current on the sample.

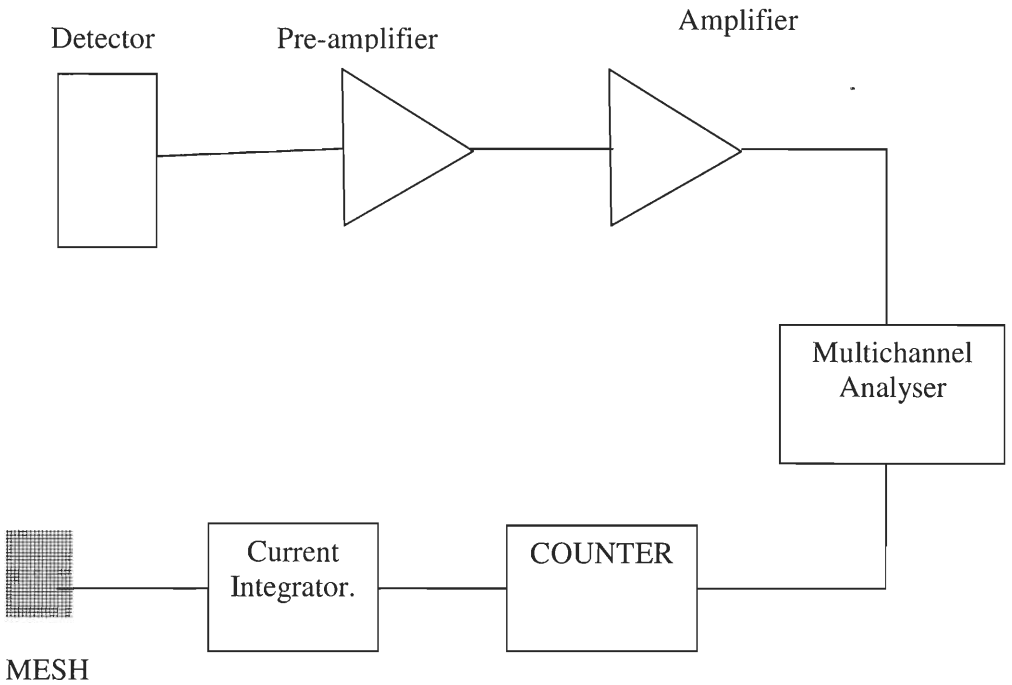

Figure 9: Data Acquisition System

CHAPTER V

THE EXPERIMENT

5.1 Analysis of the Thin Film Using RBS and NRBS

Helium (He^{++}, 2.5MeV) and the proton beams (H^{+}, 2.4MeV) were used to analyze our Ni/MgH sample. The choice of energy was made so as to obtain enhanced cross sections that are easy to quantify. Both experiments were conducted at the incident angle of 0^{o}, exit angle of 15^{o} and the scattering angle was 165^{o}. Helium beam was used to find the depth profile of Mg and Nickel. The proton beam was used to confirm the speculated presence of oxygen in the sample using NRBS. The simulated RBS spectra raised suspicion on the presence of oxygen in the sample.

Spectral data was collected for about 30000 counts on mesh for the He^{++} beam and 13505 counts for the proton beam using MAESTRO software which generates '.chn' files. These counts represent collision events that are recorded by the detector. Since the mesh has 80% transmission rate, it was deduced that there was 120000 counts on sample (He^{++} beam) and 54020 counts (H^{+} beam). Data was then converted into a compatible data by Specon software which converts to ASCII file. The data was then simulated using SIMNRA to analyze the percentage composition of magnesium, nickel and the speculated oxygen in the sample. The spectra generated by the He^{++} beam, was nicely simulated only with the inclusion of oxygen in the target. NRBS was done with H^{+} beam to confirm the hypothesis.

5.2 Simulation of RBS and NRBS Data

To simulate RBS and NRBS data, we needed three major areas of information, the *ion beam*, the *scattering geometry*, the *calibration* and *energy resolution*. RUMP software was utilized to calibrate the energy range of our spectra in SIMNRA. Our aim was to get the calibration offset (in keV) and energy per channel (keV/ch). During calibration, we also calculated the product of the solid angle (in steradians) and the number of particles scattered into that angle, Ω, using SIMNRA.

5.2.1 Calculating Solid Angle

Solid angle is given by the scattering cross section area divided by the square of the radius of the scattering configuration:

$$\Omega = A / R^2, A = \pi(\frac{d}{2})^2,$$

where d is the diameter of the scattering cross section area i.e. diameter of the detector (aperture) and R is the distance from the sample/target to the detector. Using the geometry of our scattering chamber, the aperture of our detector is 0.31750 cm While R=6.82 cm for RBS and NRBS, and R=9.3242 cm for ERD measurements.

5.2.2 Calculation of Number of Particles

The counter scale was set to 1.0×10^{-10} Coulombs. Since 1 count is equivalent to 10^{-10} Coulombs, The charge on the mesh = number of counts on mesh $\times 10^{-10}$ Coulombs. The number of particles on the mesh equals the charge on the mesh divided by the charge of the incident particle in question. For instance, H^+ beam has a charge of $+1.6 \times 10^{-19}$C per particle. The beam passes through a mesh before hitting

the sample. The mesh has 80% beam transmission. So the number of particles on sample equals the number of particles on the mesh times four.

5.3 Analysis of the Thin Film Using ERDA

The scattering geometry was as follows: The incident angle was 67.5^0 and the exit angle 67.5^0, whist the scattering angle was 45^0. An oxygen beam (O^{4+}) with 15000 keV energy was used to bombard our sample. The choice of energy was made based on the principle particle (Mg, Ni or O) apart from hydrogen should pass through the Mylar foil. SIMNRA was used to determine this energy. A graph of fractional charge vs. energy [18] for different charged oxygen atoms was used to estimate this energy value and the appropriate charge value. Initial spectral data (before sample heating) was taken for 40000 100000 and 50000 counts. The choice of 50000 counts was made for each sample heating since it gave a good statistics within a relatively short time.

5.4 Heating of the Sample

Heating was done to investigate thermal stability of Ni/MgH thin film. During the heating, the geometry of the target remained the same as with the previous ERDA measurements for reasonable comparison purposes. The heating was done using a UHV compatible non-gassy button heater. The heater was placed behind the sample and connected to the DC power supply. A k-type thermocouple was placed between the sample holder and the sample and the temperature was allowed to stabilize before the stop watch was turned on. The power supply was used to heat the sample, and the

thermocouple was there to control the heating and thus it gave us temperature values of heating.

From room temperature (21°C), the heater was initially set at 50°C. After heating to 50°C, we waited for about 15 minutes at the set temperature to heat the sample. The choice of this time was arbitrary. Afterwards, the power to the heater was disconnected and the sample was allowed to cool to room temperature and RBS and ERDA measurements were taken. Heating then continued in 25°C increments until 200°C was reached followed by the RBS and ERDA measurements after the sample had cooled down. The choice to stop heating was made based on the qualitative comparison of the ERDA spectra; it was anticipated that the equilibrium level of hydrogen had reached and most of the hydrogen had desorbed. Data collected at each temperature value was simulated using SIMNRA to quantify hydrogen loss during the heating.

5.5 Studies After Heating

5.5.1 Elastic Recoil Detection Analysis (ERDA)

Since it was observed that most of the hydrogen had desorbed at around 125°C, the sample was heated to 130°C and deuterium was fed into the chamber to test the absorption properties of the sample. The pressure inside the chamber increased from 9.0×10^{-7}Torr to 7.0×10^{-6} Torr. Deuterium was chosen for this purpose because it is an isotope of hydrogen with same electronic properties. At the same time, it becomes easy to distinguish the deuterium and the hydrogen peaks in a single ERDA experiment. In the chamber, deuterium was left to interact with the sample for

1 hour during heating. After 1 hour, heating was stopped and the deuterium valve was closed. When the sample cooled to 26°C, ERDA measurements were performed under the previous settings.

5.5.2 Backscattering Spectra After Heating

RBS and NRBS studies were conducted once again to our sample to see how much the sample profile had changed.

CHAPTER VI

RESULTS

6.1 RBS and NRBS

A simulated RBS spectrum was fitted to experimental spectrum with the incorporation of oxygen in our simulated target (Figure 10). To confirm the possibility of sample contamination by oxygen NRBS simulation clearly distinguished the three peaks from nickel, oxygen magnesium and silicon (Figure 11). The simulation indicated that our sample had indeed a considerable amount of magnesium, nickel and oxygen. Although the simulation incorporated hydrogen, it was only confirmed by ERDA results. Using IBA, thickness of the sample can be calculated if the density of the individual layers is known. In our case the compound analysis of the individual layers was not performed, therefore, the exact thickness of the sample cannot be determined. However, relative thickness of the individual layers is given by RBS as the areal density, therefore, width of the peaks in RBS spectra can be related to the thicknesses of the layers.

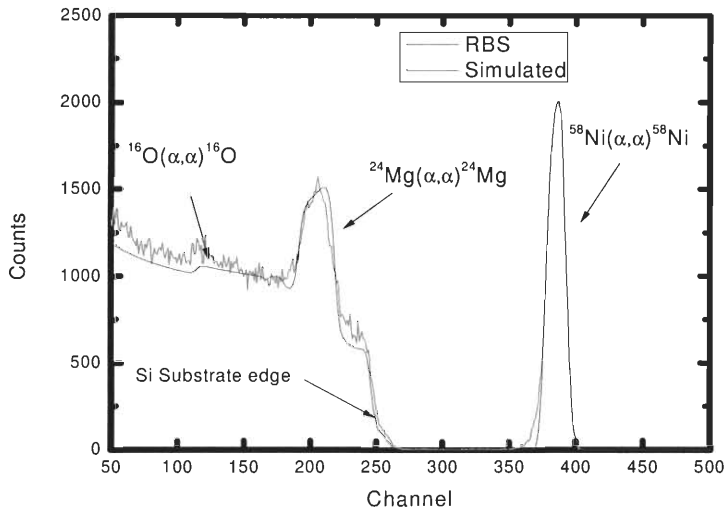

Figure 10: RBS Spectra Obtained Using (He^{2+}, 2.5MeV), Oxygen Peack Unclear

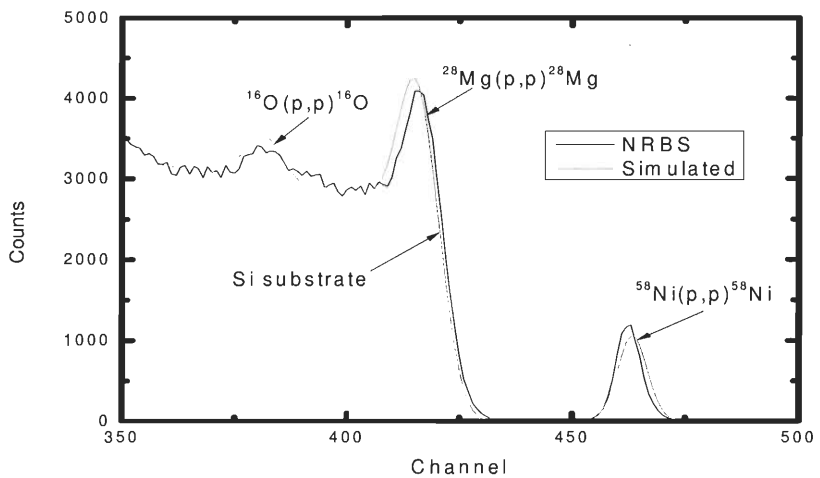

Figure 11: NRBS Spectra Obtained Using (H^+, 2.4MeV)

6.2 Thermal Stability of Hydrogen

Figure 12 shows eight spectroscopic data at each level of heating plotted for comparative purposes by Origin 8 graphing soft ware [17]. Since the area under the

peak is proportional to the amount of hydrogen in the sample, the graph can be seen as a graph of amount of hydrogen at each stage of heating. Figure 13 shows hydrogen concentration (by SIMNRA) vs. temperature. During the simulation all parameters were left constant, only target concentrations were varied. That is to say, the target for both backscattering and forward scattering remained the same. Also effort was made to keep the peak integral constant for a given data and its corresponding stimulated graph line. All integrals were taken from channel 45 to 345.

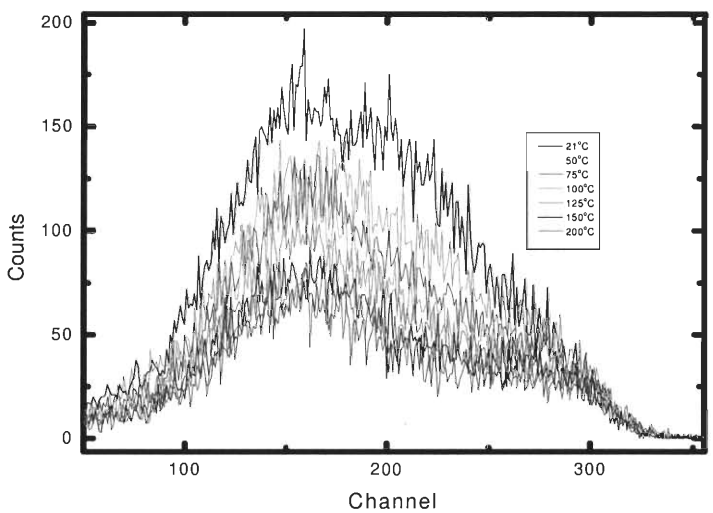

Figure 12: Overlapped Forward Recoil Spectra Obtained Using 15Mev O^{4+} Beams

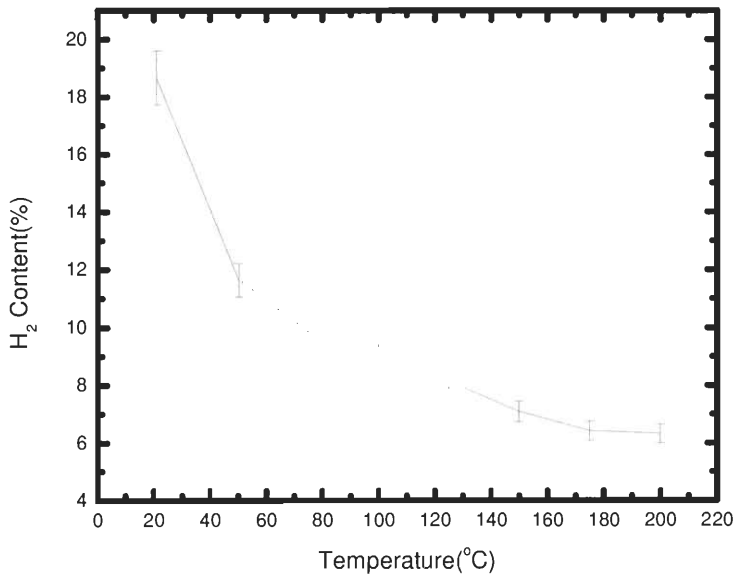

Figure 13: Variation of Percentage Hydrogen Content with Temperature

6.3 ERDA and Backscattering Spectra After Heating

A very small amount of deuterium was absorbed. However; it was not a sufficient amount for recyclability of this material (figure 14).

There was no apparent substantial change in profile of the sample spectra before and after heating (Fig. 15: graphs shifted from each other for comparison purpose).

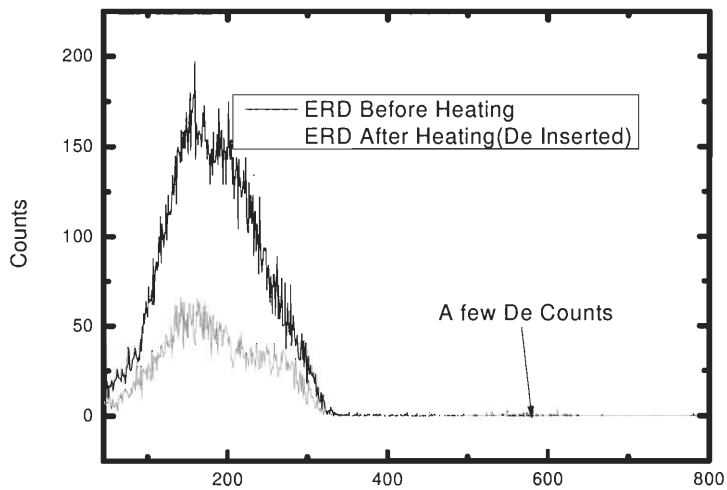

Figure 14: ERD Measurements Before and After De Insertion

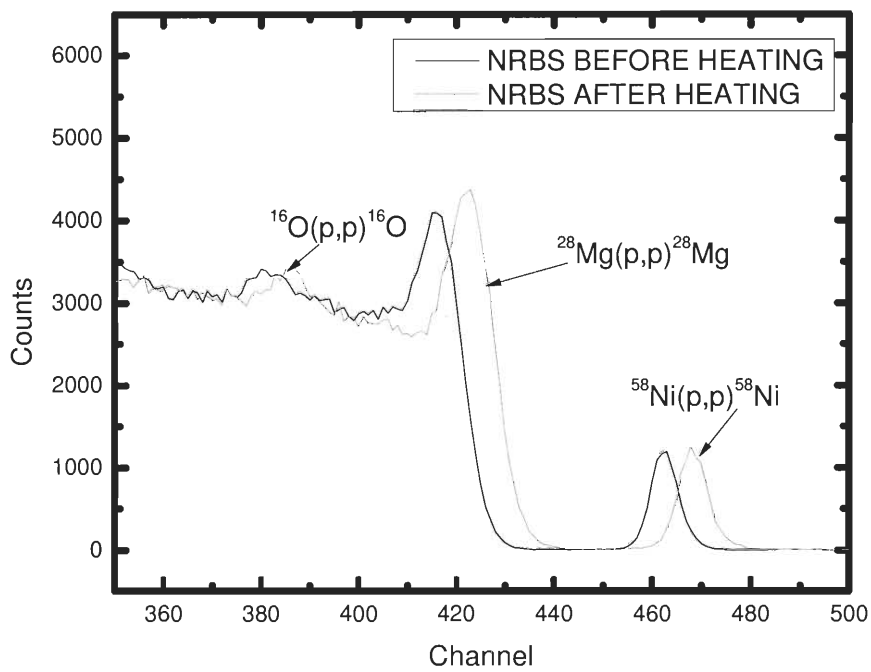

Figure 15: NRBS Before and After Heating (Spectra are Offset for Clarity)

CHAPTER VII

DISCUSSION AND CONCLUSION

7.1 Discussion

Knowledge of the temperature at which hydrogen is desorbed from the storage material helps in choosing the right material for hydrogen storage as well deducing the stoichiometry of the material. This study has shown that Ni/MgH thin film had released most of its hydrogen well at 125°C in vacuum. Figure 12 and 13 show that most of the hydrogen has been released from the sample at 125°C in vacuum. A huge amount of hydrogen was lost during the initial heating (from 21°C to 50°C) which raises suspicion for the presence of more than one phase of MgH. A relatively low amount of hydrogen was lost during the second stage of heating (from 50°C to 75°C). From 75°C onwards, there was a gradual hydrogen loss until around 150°C where the graph line roughly remains constant. There was still an appreciable amount of trapped hydrogen that could not be desorbed even at 200°C. The presence of this trapped hydrogen may be attributed to the presence of a phase with strongly bonded hydrogen among other possibilities. Nevertheless, the thermal stability curve indicates that the sample could release most of its hydrogen at a reasonably low temperature. This seems good because MgH_2 releases hydrogen at around 300°C [6] as far is experiment with bulk materials is concerned. The campaign for hydrogen storage materials targets the realization of an optimum temperature for hydrogen release from a particular storage material [5]. Simultaneously, hydrogen storage requires that the material used

should have good recycling properties. That is, the material must have a high capacity to release and reabsorb most of its hydrogen. Consequently a good material is deemed as recyclable if it can release and absorb hydrogen at a reasonable temperature for continuous usage. Ni/MgH sample could not absorb enough deuterium despite absorbing a lot of hydrogen.

As previously noted, there are factors which hinder the diffusion of hydrogen in and out of the material, the main culprits being oxidation and creation of hydride layer on the surface of the material [4, 11]. The second spectrum (Figure 11) shows that our sample contains oxygen apart from Mg, H, and nickel elements. This indicates that our sample is contaminated with oxygen which might negatively affect deuterium absorption. This might be likely due to the oxidation of the sample during transfer from the PVD chamber to the scattering chamber, and possibly during the connection of the button heater. This deduction comes in due to the fact that Mg reacts well with oxygen to form MgO based on the electron configuration of the two elements. This may be a challenge to our hydrogen storage sample material since the ideal one is intended to work in the normal atmospheric air in which oxidation is likely to be a huge problem. It is not clear whether the hydride layer was created on the surface of Ni/MgH or not. Otherwise if it was, it might have as well contributed to the reduced deuterium implantation.

Obviously contamination by oxygen explains our inability to incorporate deuterium in the sample at an appreciable amount of sample heating of 130^{o}C. We deposited nickel on top of the MgH with the assumption that this might prevent

oxidation or any other coating that might hinder hydrogen diffusion in our sample and also act as a catalyst to dissociate from molecular deuterium or hydrogen to atomic. While it was relatively easy to dissociate hydrogen from Ni/MgH in our experiment to ensure sample recyclability, it was impossible to deduce whether deuterium entered our material as seen from the small deuterium signal (Figure 14). Since we noticed an appreciable amount of hydrogen in our sample (Figure 13) and that a great deal of H_2 had already desorbed at temperature as low as 125°C (Figures 12 and 13), we suggest that future research be directed to the recyclability of this material. More work can also be done to inquire about the structure of this material as well as its thermal stability in an atmospheric environment since the final hydrogen storage material will be in operation in an atmospheric condition.

7.2 Conclusion

This study has indicated that Ni/MgH deposited on a silicon substrate, has a potential to lose most of its hydrogen if heated to a temperature of about 125°C in vacuum. The sample deposition parameters proved to be carefully chosen as shown by the huge percentage of hydrogen in the sample. In this study it has been shown that deuterium adsorption proved to be impossible at 130°C. This leaves the question of recyclability of the sample unsolved. Future studies on the improvement of deuterium adsorption on such samples and the thermal stability of this material in the atmosphere are recommended. Additionally, future research may also be carried out to dissociate extra hydrogen that was still trapped in the sample after a series of sample heating to a maximum temperature of 200°C.

BIBLIOGRAPHY

[1].E. David, An overview of advanced materials for hydrogen storage 13th International Scientific Conference on Achievements in Mechanical and Materials engineering 16th -19th May 2005.

[2].W. Luo, J. Alloys and Compounds, 381 (2004) 284-287

[3].C.M.Jensen, R.Zidan, N.Mariels, A.Hee, C.Hagen, INT.J. Hydrogen Energy, 24,461, (1999);

[4].B. Sakintuna, F. Lamaridarkrim, M. Hirscher, *International Journal of Hydrogen Energy* **32**, 1121-1140 (2007).

[5].DOE: us Department of Energy. Website:http://www.doe.gov)

[6].M. Dornheim, S. Doppiu, G. Barkhordarian, U. Boesenberg, T. Klassen, O. Gutfleisch and R. Bormann, Scripta Materialia 56 (2007) 841–846

[7].Zaluska A, Zaluski L, Stromm-Olsen JO. Nanocrystalline magnesium for hydrogen strorage. J Alloys Compds 1992;288:217-25.

[8].Barkhordarian G, Klassen, T, Bormann R. Effect of Nb2O5 content on hydrogen reaction kinematics of Mg. J Alloys Compds 2004;364:242-6.

[9]. J. Huot, G. Liang, S. Boily, A. Van Neste, R. Schulz Journal of Alloys and Compounds 293–295 (1999) 495–500

[10].http://www.southern-pvd.com/download/Introduction.pdf

[11].A. Dissanayake, S. AlFaify, E.Garratt, M.I.Nandasiri, R. Taibu, G. Tecos, N.M.hamdan and A. Kayani, Measurement Of Hydrogen Capacities And Stability

In Thin Films Of AlH Deposited By Magnetron Sputtering, accepted to publish in AIP Conf. Proc.1336, 189-192(2011)

[12].J. Kennedy & A. Markwitz Characterisation Of ZnO Films by Ion Beam Analysis International Journal of Modern Physics B (2006) Vol. 20, Nos. 25, 26 & 27 4655-4660

[13].U.V. Toussaint, K. Krieger, R. Fischer, V. Dose. Depth Profile Reconstruction From Rutherford Backscattering Data. Max-Planck-Instut fur plasmaphysik (n.d): Garching, Germany.

[14].M. Dobeli, Material Analysis, Paul Scherrer Institute and ETH-Zurich, Switzerland,Retrievedfrom: http://cas.web.cern.ch/cas/Pruhonice/PDF/Doebeli.pdf

[15].M. Mayer. Rutherford Backscattering Spectrometry (RBS). Max-Planck-Institut f¨ur Plasmaphysik, EURATOM Association, Garching, Germany Lectures given at the Workshop on Nuclear Data for Science and Technology: Materials Analysis Trieste, 19-30 May 2003

[16].M. Mayer, SIMNRA User's Guide, Technical Report IPP9/113, Max-Planck-Institut fur Plasmaphysik, Garching, Germany (1997)

[17].Origin 8 SR1. Origin Lab Corporation. 1991-2007

[18].S.M. Ferguson. Equilibrium Charge State Distributions of Heavy Ions in Carbon. Research School of Physical Sciences, The Australian National University, Canberra, June, 1974

[19].J.Larminie & A. Dicks. *Fuel Cell Systems Explained* (2nd Ed.). (2003). John Willey & Sons Ltd.

[20].J.R.Tesmer, M.Nastasi, Handbook of Modern Ion Beam Materials Analysis, Materials Research Society, Pittsburgh, PA, 1995

[21].Advanced Materials Analysis Facility at CSIRO HIAF Laboratory. *www.iaea.org/inis/collection/NCLCollectionStore/_Public/.../28027216.pdf*

[22].Weast RC, Astle MJ, Beyer WH. CRC handbook of chemistry and physics. 64th ed., Boca Raton, FL: CRC Press; 1983.

[23].Grochala W, Edwards PP. Thermal decomposition of the non-interstitial hydrides for the storage and production of hydrogen. Chem Rev 2004; 104:1283-315.

[24].Fukai Y. The metal-hydrogen system, basic bulk properties. Springer series in materials science, 1993.